Catalysis Today 288 (2017) 30–36

Contents lists available at ScienceDirect

Catalysis Today

journal homepage: www.elsevier.com/locate/cattod

Size-dependent reactivity of gold-copper bimetallic nanoparticles during CO_2 electroreduction

Hemma Mistry[a,b], Rulle Reske[c], Peter Strasser[c], Beatriz Roldan Cuenya[b,*]

[a] Department of Physics, University of Central Florida, Orlando, FL 32816, United States
[b] Department of Physics, Ruhr-University Bochum, 44780 Bochum, Germany
[c] Department of Chemistry, Chemical Engineering Division, Technical University Berlin, 10623 Berlin, Germany

ARTICLE INFO

Article history:
Received 6 July 2016
Received in revised form 2 September 2016
Accepted 11 September 2016
Available online 6 October 2016

Keywords:
CO_2 electroreduction
Nanoparticle
Size effect
Gold
Copper
Bimetallic

ABSTRACT

New catalysts are needed to achieve lower overpotentials and higher faradaic efficiency for desirable products during the electroreduction of CO_2. In this study, we explore the size-dependence of monodisperse gold-copper alloy nanoparticles (NPs) synthesized by inverse micelle encapsulation as catalysts for CO_2 electroreduction. X-ray spectroscopy revealed that gold-copper alloys were formed and were heavily oxidized in their initial as prepared state. Current density was found to increase significantly for smaller NPs due to the increasing population of strongly binding low coordinated sites on NPs below 5 nm. Product analysis showed formation of H_2, CO, and CH_4, with faradaic selectivity showing a minor dependence on size. The selectivity trends observed are assigned to reaction-induced segregation of gold atoms to the particle surface and altered electronic or geometric properties due to alloying.

1. Introduction

Alloying is a powerful technique to improve the reactivity of metal nanocatalysts by influencing their morphological, chemical, and electronic properties [1–3]. For example, adding a second metal can induce strain or changes in the electronic structure of a catalyst, altering the interaction of reactive species with its surface [4]. Alternately, a secondary metal may provide an alternative active site which facilitates a different reaction step or works as an isolated active site [5]. One reaction where alloyed catalysts may provide remarkable improvement in catalyst activity and selectivity is the electroreduction of CO_2. Currently, Cu shows the most promise as a catalyst for this reaction since it can produce hydrocarbons, but only at high overpotentials [6–9]. Au is also a promising material since it can selectively generate CO at moderate overpotentials [10,11]. Despite these results, low-cost catalysts with high selectivity and efficiency for CO_2 reduction to valuable products are yet to be discovered.

Using density functional theory (DFT), Hansen et al. have shown that the unique hydrocarbon selectivity of Cu can be linked to its optimal binding to the CO* and COOH* intermediates in comparison to other metals [12]. These results indicate that the reactivity of Cu could be further improved by tuning its binding properties to different intermediates, although the scaling relations between these binding energies must first be broken [13]. Several strategies for achieving this have been proposed, including nanostructuring the Cu surface [14] or adding ligands to an active metal center [15], but the most promising may be introducing a secondary metal to create an alloy catalyst [13,16].

Recently, several experimental and theoretical studies have explored the reactivity of bimetallic catalysts during CO_2 electroreduction [5,17–26]. In particular, several studies have focused on copper-gold bimetallics, due to the reactivity of both of these metals [18,27–36]. Composition dependent studies on bulk Au-Cu alloys and 10 nm Au-Cu nanoparticles (NPs) indicate that hydrocarbon production is favored with increasing Cu content, although not surpassing that of pure Cu, while increasing Au content favors an increase in CO selectivity [29]. In order to understand the reactivity of AuCu bimetallic catalysts, it is crucial to understand the structure and stability of the catalysts during the reaction. Monzó et al. investigated Au core Cu shell NPs for CO_2 electroreduction, arguing that trends in reactivity may be explained by strain effects in the Cu shells of different thickness [31]. However, it is important to consider that Cu monolayers on an Au surface can be highly unstable under electrochemical conditions, and Au may segregate to the surface and alloy with Cu [30,37]. In addition, previous stud-

* Corresponding author.
E-mail address: Beatriz.Roldan@rub.de (B. Roldan Cuenya).

http://dx.doi.org/10.1016/j.cattod.2016.09.017
0920-5861/

ies on AuCu CO_2 electroreduction catalysts have been restricted to bulk-like surfaces [27,35] or NPs 10 nm or larger in size [29,31–33], although NPs smaller than 10 nm are known to have widely different reactivity than their bulk counterparts [38,39]. It is also important to consider the oxidation state of the metals in the NP surface and its evolution during the reaction, since oxide derived Cu nanostructures have shown widely improved reactivity during CO_2 electroreduction [40], and a secondary metal may alter the stability of such oxides.

In this study, we address the structure-dependent reactivity of AuCu bimetallic NPs for CO_2 electroreduction using well-defined model NP catalysts less than 10 nm in size. NPs in the size range from 1.4 to 24 nm were synthesized using inverse micelle encapsulation and characterized using microscopy and X-ray spectroscopy. Although a significant increase in activity was found for smaller NPs, the selectivity was found to have only slight size dependence, in stark contrast to monometallic Au and Cu NPs.

2. Experimental

2.1. Nanoparticle synthesis

Monodisperse AuCu bimetallic NPs were synthesized using the inverse micelle encapsulation technique. Poly(styrene-*b*-2-vinyl pyridine) diblock copolymers (Polymer Source, Inc.) with different molecular weights (Table 1) were dissolved in toluene to form reverse micelles. $HAuCl_4$ and $CuCl_2$ were added to the solutions and stirred for two days. The resulting metal loaded micelle solutions were dip-coated onto the support (silicon wafers or glassy carbon), and then the encapsulating polymers were removed using 20 min of oxygen plasma at 20 W. The absence of the C 1 s signal in X-ray photoelectron spectra (XPS) measured on silicon wafer-supported samples was used to ensure the plasma etching conditions were sufficient to completely remove the polymers. For the synthesis of the electrodes, the dip-coating and plasma etching steps were repeated three times to increase the loading of NPs on the glassy carbon.

2.2. Structural and chemical characterization

Atomic force microscopy (AFM) was used to determine NP size, interparticle distance, and geometrical surface area of our NP catalysts. AFM was acquired using a Digital Instruments Nanoscope-III microscope on ligand-free AuCu NPs dip-coated onto SiO_2/Si(111) wafers. The interparticle distance d was estimated as $d = \frac{1}{\sqrt{\sigma}}$ by measuring the NP density σ and assuming hexagonal arrangement. The metal NP surface area was estimated by using the NP height and NP density from AFM and calculating the NP surface area per area of support, assuming spherical NPs. The latter was used as geometrical metal surface area for the normalization of the electrochemical currents.

XPS was measured with a monochromatic Al Kα source (1486.6 eV) in an ultra-high vacuum (UHV) system with 2×10^{-10} mbar base pressure (Phobios 150, SPECS GmbH). Data were aligned to the Si^0 2p peak at 99.3 eV. X-ray absorption fine-structure spectroscopy (XAFS) was measured at beamline 10-ID-B of the Advanced Photon Source at Argonne National Laboratory. For XAFS, 7.9 nm AuCu NPs supported on a carbon foil were measured in air in fluorescence geometry at the Cu K and Au L_3 edges. Data were analyzed using the Athena and Artemis software from the IFEFFIT package [41], and fitting was performed using FEFF 8 calculations [42].

2.3. Electrochemical methods

CO_2 electroreduction was performed in a three electrode electrochemical cell. A platinum mesh 100 was used as counter electrode, and a leak-free Ag/AgCl electrode was used as reference electrode. The working electrode was the AuCu NPs supported on glassy carbon plates. The electrolyte was 0.1 M $KHCO_3$, and CO_2 was bubbled at a constant flow rate of 30 mL/min from the bottom of the cell (pH = 6.8). Every measurement was started with a linear voltammetric sweep performed with a scan rate of −5 mV/s between E = +0.05 V_{RHE} and the working potential (−1.2 V_{RHE}), followed by a chronoamperometric step for 10 min. Gas products (H_2, CO, and CH_4) were monitored using a gas chromatograph (Shimadzu GC 2016) equipped with a thermal conductivity detector (TCD) and a flame ionization detector (FID). The products were measured at −1.2 V_{RHE} to ensure high enough production rates for reliable GC detection over our low loading samples. The signal from a blank glassy carbon electrode was subtracted from all electrochemical data shown here.

3. Results and discussion

For this study, AuCu NPs ranging from 1.4 to 24 nm in size were synthesized using an inverse micelle encapsulation method. Since the surface of the glassy carbon electrodes is rough, the NPs were deposited onto silicon wafers to accurately characterize their morphology using AFM. Fig. 1 and Fig. S1 in the Supplementary material show AFM images of three coats of AuCu NPs supported on SiO_2/Si(111), with size histograms shown in Fig. S2 in the Supplementary material. Table 1 lists the synthesis parameters used for the five samples, along with the morphological parameters acquired from AFM including the NP size, interparticle distance, and the surface area used for normalization of the electrochemical data. The AFM results show that the NPs could be synthesized with a high degree of size control, and narrow size distribution was achieved for the four smaller NP sizes. The largest 24 nm NPs had a wider size distribution and resulted in a bimodal size distribution, as shown in Fig. S2e in the Supplementary material. Further discussion of this sample is given in the Supporting information.

XPS was used to characterize the composition and chemical state of the NPs in their initial as prepared state. The composition of the NPs was determined by quantifying the Au 4f and Cu $2p_{3/2}$ peaks measured on the as prepared NPs supported on SiO_2/Si(111). Close to 50-50 Au-Cu composition was calculated for each sample, as shown in Table 1. It should be noted that XPS is a surface sensitive technique and may not probe the bulk of the larger NPs.

XPS was also used to investigate the oxidation state and alloying of the Au and Cu in the NPs. Fig. 2 shows the Au 4f and Cu 2p core level regions measured on the 7.9 nm AuCu NPs supported on SiO_2/Si(111). Fig. 2a and b shows data acquired immediately after *ex situ* O_2 plasma treatment and transfer in air to the UHV system for XPS measurement. After O_2 plasma, the Au 4f region shows mainly Au^{3+} peaks, indicating that the NPs contained mostly Au_2O_3 species. Small Au^0 peaks were also measured, and the Au^0 $4f_{7/2}$ peak agrees with bulk metallic gold at 83.9 eV. The Cu 2p region shows only Cu^{2+} species with the characteristic satellite peaks at higher binding energies. Only the Cu $2p_{3/2}$ peaks were fit, since a sloped background exists at high binding energies due to overlap with the O LMM Auger lines. The Cu $2p_{3/2}$ peak can be deconvoluted into two peaks which agree with CuO and $Cu(OH)_2$ species. These results show that the NPs are heavily oxidized in their as prepared state due to the O_2 plasma treatment employed during the synthesis.

In order to confirm that true alloyed NPs were formed, the oxidized NPs were thermally reduced under mild reducing conditions

Table 1
Synthesis parameters and size characterization of bimetallic AuCu NPs prepared via inverse micelle encapsulation: polymer size, loading (metal salt to P2VP ratio), NP size measured from AFM, metal surface area assuming spherical NPs (cm^2 of metal per cm^2 of support), interparticle distance, and NP composition derived from XPS.

Polymer Weight	Loading	NP Size (nm)	Surface Area	Interparticle Distance (nm)	Composition
PS(9800)–P2VP(17,000)	0.1	1.4 ± 0.7	0.0458	12.9	$Au_{48}Cu_{52}$
PS(43,800)–P2VP(53,000)	0.2	4.8 ± 1.2	0.100	27.7	$Au_{60}Cu_{40}$
PS(46,000)–P2VP(33,000)	0.2	5.6 ± 1.3	0.107	31.4	$Au_{34}Cu_{66}$
PS(70,000)–P2VP(48,500)	0.2	7.9 ± 1.7	0.148	37.4	$Au_{63}Cu_{37}$
PS(135,000)–P2VP(130,000)	0.4	24 ± 6	0.145	75.7	$Au_{44}Cu_{56}$

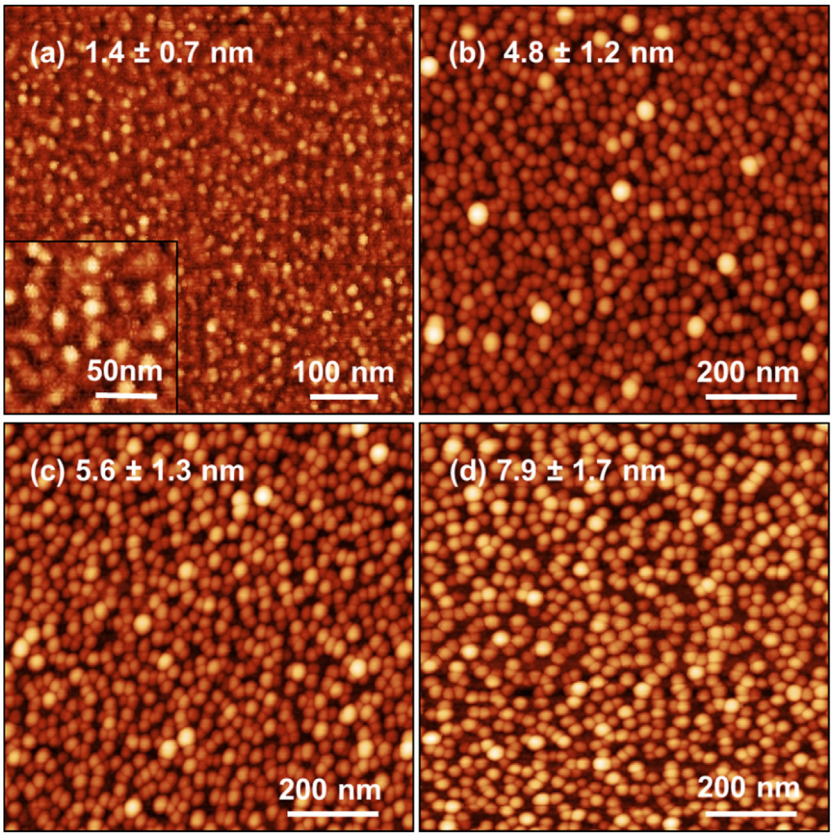

Fig. 1. AFM images of bimetallic AuCu NPs supported on SiO_2/Si(111). (a) 1.4 ± 0.7 nm (enlarged region shown in inset), (b) 4.8 ± 1.2 nm, (c) 5.6 ± 1.3 nm, and (d) 7.9 ± 1.7 nm.

in situ so that binding energy shifts due to alloying could be detected with XPS. XPS was measured on the 7.9 nm AuCu NPs/SiO_2/Si(111) after annealing *in situ* for 20 min at 275 °C in UHV. Fig. 2c and d shows the Au 4f and Cu 2p regions of the sample after *in situ* reduction. The Au 4f region in Fig. 2c shows that the Au has been reduced to metallic Au, with an Au $4f_{7/2}$ binding energy of 84.0 eV. The Cu 2p region also shows reduction of the Cu^{2+} species with a Cu $2p_{3/2}$ peak binding energy of 932.3 eV. A negative binding energy shift exists with respect to bulk metallic Cu at 932.7 eV. Bulk alloys of Au and Cu have shown a positive binding energy shift of 0.1 to 0.5 eV in Au 4f, and a negative shift of approximately 0.1 to 0.4 eV in Cu 2p [43]. The positive binding energy shifts in Au 4f are due to transfer of d charge from Au to Cu, although overall Au gains charge due to its electronegativity. Similarly, Cu gains d charge causing the negative binding energy shifts in Cu 2p [43]. Therefore, our results indicate that Au-Cu alloyed NPs were synthesized.

The 7.9 nm AuCu NPs were also supported on carbon foil and measured in their oxidized as prepared state using XAFS to gain information on the structure and chemical state. Fig. 3 shows XANES and EXAFS of this sample measured at the Cu K and Au L_3 edges. The XANES spectrum at the Cu K edge (Fig. 3a) shows the features of CuO species, in agreement with XPS measurements. Table 2 and Fig. 3b show fit results for the Cu K edge EXAFS. EXAFS fitting gave a Cu—O bond distance of 1.95 ± 0.01 Å, also in good agreement with CuO structure. No Cu—Cu bonds could be fit, indicating the copper in the NPs was heavily oxidized. The Au L_3 edge XANES spectrum of the sample, shown in Fig. 3c, shows a white line feature indicating the presence of Au^{3+} species in Au_2O_3. Fit results for the Au L_3 EXAFS are also given in Table 2 and plotted in Fig. 3d, indicating an Au-Au path with coordination number (CN) 10, and an Au-O path with CN = 0.6. In agreement with XPS, XAFS measurements revealed that the initial samples are heavily oxidized and likely initially composed of segregated oxidized Au and Cu grains, since no AuCu path could be fit.

Table 2
EXAFS fit parameters: coordination number (CN), bond length (r), and disorder parameter (σ^2) for the Cu K edge and Au L_3 edge of as prepared 7.9 nm AuCu NPs supported on carbon foil.

Path	CN	r(Å)	σ^2 (10^{-3} Å^2)
Cu—O	3.2 ± 0.5	1.95 ± 0.01	2 ± 2
Au—Au	10 ± 1	2.854 ± 0.007	9 ± 1
Au—O	0.6 ± 0.2	2.00 ± 0.03	1 ± 4

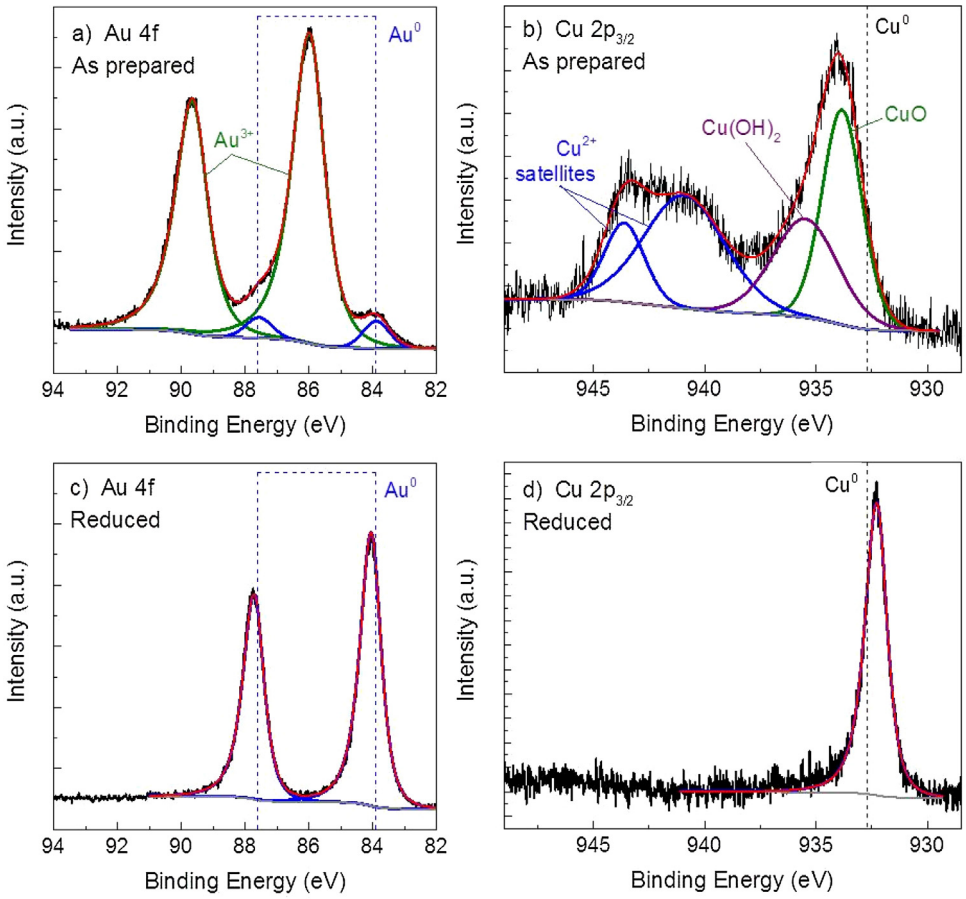

Fig. 2. XPS data of the (a,c) Au 4f and (b,d) Cu 2p core level regions of 7.9 nm AuCu NPs supported on SiO_2/Si(111). The spectra were measured of the same sample in its as prepared state (a,b), and after *in situ* reduction (c,d).

The AuCu NPs supported on glassy carbon were used as the working electrode for the electroreduction of CO_2 in 0.1 M $KHCO_3$. Fig. 4 shows the current density after the first 10 min of reaction for each sample as a function of NP size. A significant increase in activity with decreasing NP size was observed, with the smallest 1.4 nm NPs showing approximately twice the current density of the largest NPs. This trend is in agreement with previous studies on monometallic Au and Cu NPs, where CO_2 reduction current density increased significantly with decreasing NP size, particularly below 5 nm NP size [38,39]. In those studies, the size dependent trend was due to the increased population of low coordinated sites on the smaller NPs, which were more active. It is likely that a similar mechanism can explain the size-dependent activity here. The 5.6 nm NPs are slightly out of the trend, showing a larger current density than the 4.8 nm NPs which are closest in size. This anomaly may be related to the differing composition of these two samples, which will be discussed below.

The selectivity towards gas products was measured at −1.2 V *vs.* RHE using gas chromatography and is plotted in Fig. 5. The NPs show ~20% selectivity for CO_2 reduction products (CO and methane), and the remaining selectivity is to H_2. Fig. 5a shows that the production of H_2, CO, and CH_4 increases for smaller NPs, however Fig. 5b shows that there is only very small size dependent change in the Faradaic selectivity for different products. CO selectivity increases from approximately 11% on the smallest NPs to 18% on the largest NPs, while CH_4 selectivity remains roughly constant with size. These trends are in stark contrast to monometallic Au and Cu NPs, which show drastic size-dependent changes in product selectivity [38,39,44,45].

Our results demonstrate that while activity is strongly dependent on NP size, selectivity does not show a strong size-dependence. This result can be compared to size-dependent studies from our group on similarly prepared mono-metallic Au and Cu NPs during CO_2 electroreduction, which clearly show size dependent selectivity [38,39]. Cu NPs were shown to have increasing selectivity towards hydrocarbons for larger NP sizes, while smaller NPs favorably produced H_2 and CO. In comparison, for Au NPs, CO selectivity increased with increasing NP size, while H_2 selectivity decreased. The trends in H_2 and CO selectivity in our AuCu catalysts follow the trends we observed for pure Au NPs, although CO selectivity is not as high for the bimetallic NPs in comparison to the pure Au. This trend may indicate that the surface of the AuCu NPs is Au rich. In our previous work on micellar Au NPs, DFT calculations showed under the high H* coverage that is likely present on the NP surface under CO_2 electroreduction conditions, H_2 evolution becomes more facile than CO_2 reduction on low coordinated surfaces, i.e. Au(211) versus Au(111) [38]. A similar mechanism may explain the higher H_2 selectivity of our smallest AuCu NPs, since low-coordinated Au atoms on an Au-rich surface of AuCu NPs may also favor H_2 evolution. DFT has also predicted that adsorbed CO will enhance the hydrogen evolution reaction on close-packed metal surfaces due to repulsion between CO* and H* [46].

In order to understand the size-dependent selectivity, it is critical to also consider the drastic chemical and structural changes that may occur in these bimetallic NPs under reaction conditions [17,36,47–50]. In particular, several studies have shown that such drastic restructuring can occur in bimetallic catalysts under CO_2 electroreduction conditions [24,25,30,51]. In their initial state, the AuCu NPs are oxidized due to the O_2 plasma treatment, and it is

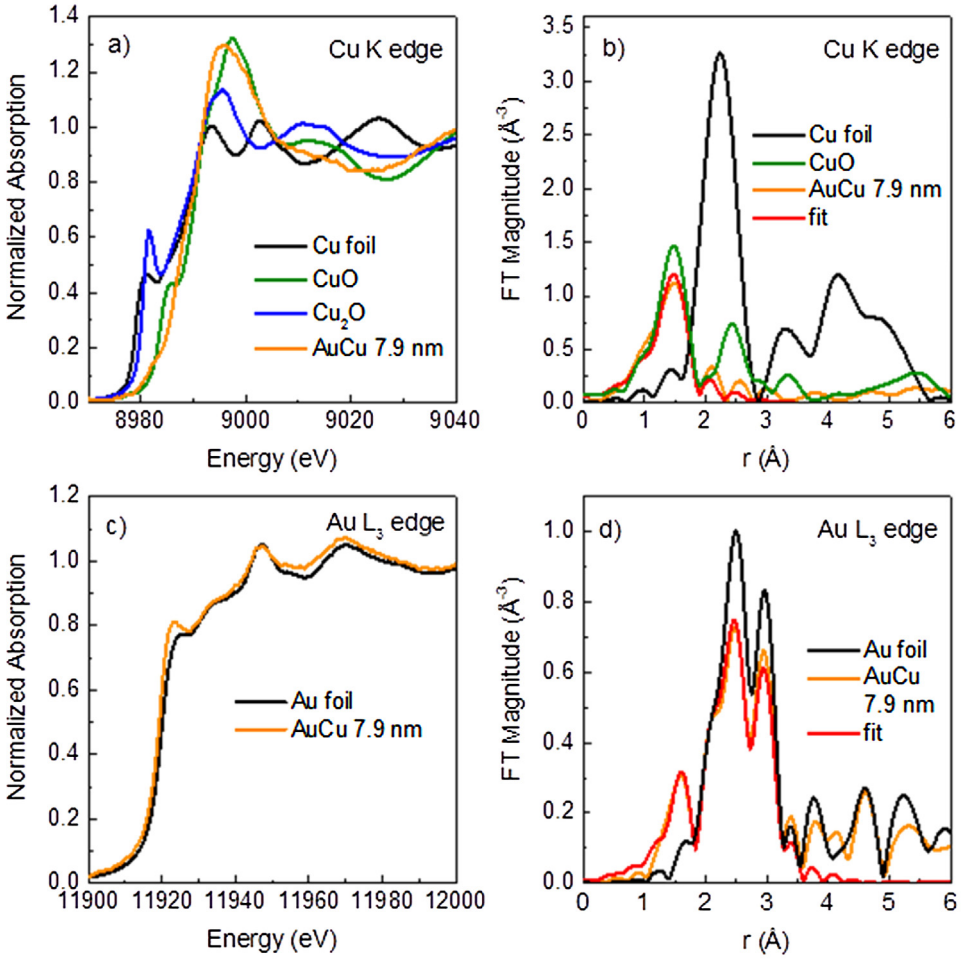

Fig. 3. XAFS measurements of as prepared 7.9 nm AuCu NPs supported on carbon foil. (a) XANES spectrum of the AuCu NPs and bulk Cu foil, CuO and Cu_2O references at the Cu K-edge. b) k^2-weighted EXAFS spectrum of Cu references, AuCu NPs, and fit at the Cu K edge (Fourier transform k range 2.5–10.5 Å). c) XANES spectrum of the AuCu NPs and Au foil at the Au L_3 edge. d) k^2-weighted EXAFS spectrum of Au foil, AuCu NPs, and fit at the Au L_3 edge (Fourier transform k range 2.5–12 Å).

favorable for Cu to segregate to the surface under oxidizing conditions, due to its higher affinity for oxygen. Consequently, it is possible that the initial NPs have a Cu oxide-rich surface. Other studies of AuCu catalysts have also shown that Cu can segregate to the surface after air exposure, after calcination, or during oxidation reactions [52–55]. During the reaction at the high overpotential used for CO_2 electroreduction, the NPs are expected to become at least partially reduced, and under these reducing conditions it is more favorable for Au to segregate to the surface, due to its lower surface energy and larger atomic radius. Indeed, Friebel et al. have shown that Cu monolayers on Au(111) undergo restructuring and alloying with the underlying Au due to segregation of Au atoms to the surface under electrochemically reducing conditions [30]. Furthermore, EXAFS measurements of AuCu clusters in a reducing H_2 environment have also indicated segregation of Au to the surface [56]. Similarly, it is possible that the surface of our AuCu NPs is Au-rich under reaction conditions, which could explain the higher selectivity towards CO as opposed to CH_4 and the absence of C_2H_4.

Studies of composition dependence in bulk and 10 nm NP AuCu catalysts have shown that increasing Au content increases the selectivity towards CO compared to hydrocarbons [27,29]. Similarly, for our AuCu NPs, which may be Au-rich at the surface, the majority of the CO_2 reduction selectivity is towards CO, while only ~3% CH_4 selectivity is observed. The 5.6 nm NPs were observed to have slightly higher methane selectivity and lower CO selectivity compared to 4.8 nm NPs, which are very similar in size, which may be due to their bulk composition being Cu rich. This Cu-rich sample also shows the highest methane production, in line with the results from Kim et al., who show that no methane is produced on their $Au_{50}Cu_{50}$ catalysts, whereas 4% methane is produced on $Au_{25}Cu_{75}$ at ~−1.1 V *vs.* RHE. Furthermore, their Cu rich catalyst showed lower CO selectivity in comparison to a sample with the same size but 50-50 Au-Cu composition [29].

Another factor to consider is the reduction of the oxidized NP surfaces, which may create unique highly active sites for CO_2 electroreduction. Previous work has shown that bulk Cu surfaces which are oxidized and reduced show higher activity, lower overpotentials, and higher selectivity towards CO or C_2H_4 with suppression of CH_4 in comparison to metallic Cu [40,57–61]. Similarly, oxidized and reduced Au surfaces have shown vastly improved CO_2 reduction behavior compared to metallic Au [62]. Our group has recently shown that the improved catalytic reactivity of oxide-derived Cu is not only due to the highly rough surfaces which are created during the oxidation and reduction treatment or the high local pH generated by the high currents on these rough surfaces, but also by the survival of cationic Cu species and subsurface oxygen within the catalyst which control the selectivity and low overpotential for CO_2 reduction [61]. The AuCu NPs used in this study are heavily oxidized in their initial state, and would become partially or fully reduced under reaction conditions.However, it is unlikely that oxide species

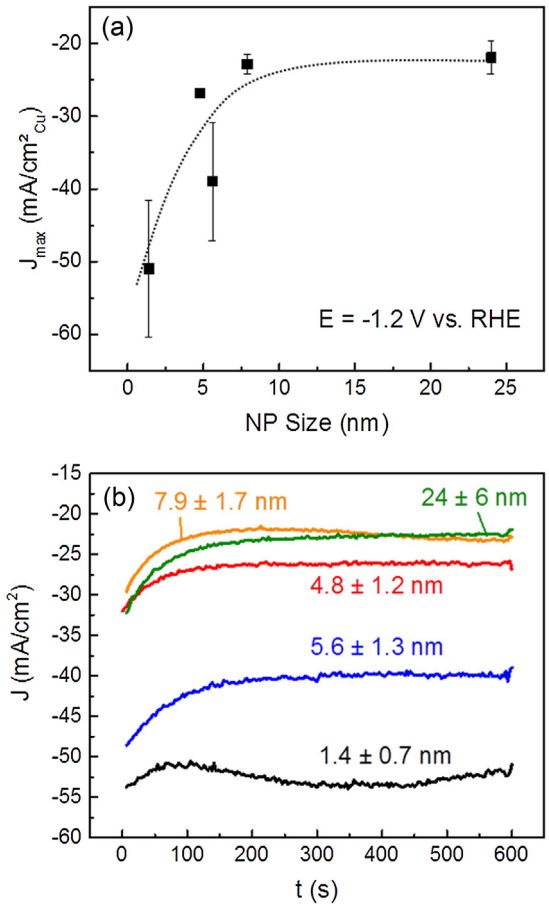

Fig. 4. a) Current density after 10 min of reaction during CO_2 electroreduction at E = −1.2 V *vs.* RHE. Error bars indicate the standard deviation of multiple measurements on analogously prepared fresh independent samples. The dashed line is a guide for the eye. b) Chronoamperometry during the first 10 min of reaction at −1.2 V *vs.* RHE.

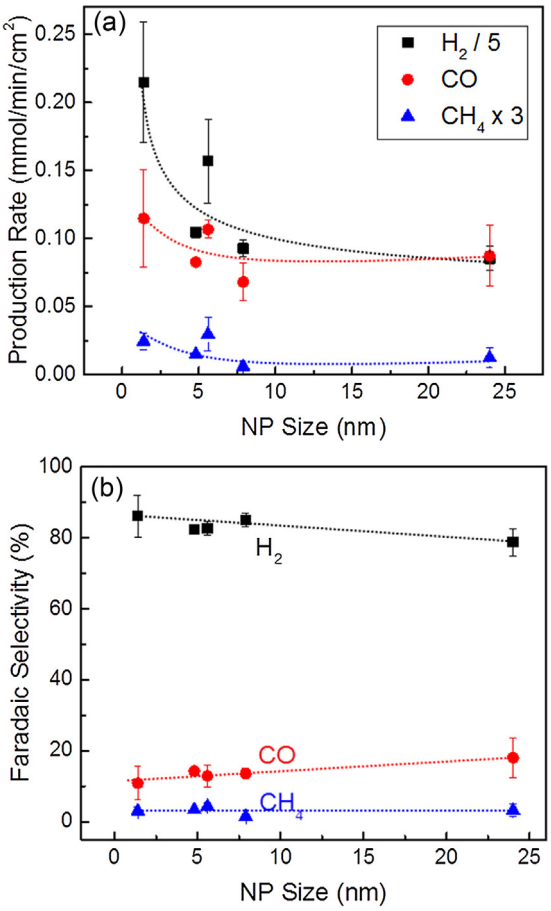

Fig. 5. (a) Molar production rate and (b) Faradaic selectivity towards gas products formed during CO_2 electroreduction as a function of NP size. Error bars indicate the standard deviation of multiple measurements carried out on analogously prepared independent fresh samples. Dashed lines are guides for the eye.

can survive in these small NPs at CO_2 electroreduction overpotentials, in contrast to the thick bulk oxidized surfaces. In addition, we do not see C_2H_4 production or high CO selectivity, which are the signatures of oxide-derived catalysts. In this case, a plausible explanation for the trends observed is that, even if Cu^+ species might be more stable on the Cu-Au NPs than in other related systems such as Cu-Pd or Cu-Ni due to the low affinity of Au for O [63], the concomitant favorable Au surface segregation results in the absence of Cu^+ at the NP surface. Therefore, even if Cu^+ species might remain stabilized on these NPs under reaction conditions, they should be subsurface and therefore not directly exposed to the reactants.

4. Conclusion

Bimetallic $Au_{0.5}Cu_{0.5}$ NPs 1.4–24 nm in size were synthesized using inverse micelle encapsulation to achieve narrow size distribution. X-ray spectroscopy revealed that the NPs were oxidized in their initial state. Smaller NPs showed high current density during CO_2 electroreduction due to their higher population of low coordinated sites at the surface. Faradaic selectivity depended less strongly on NP size. For all NPs, H_2 was the dominant product with approximately 80% selectivity, although CO and CH_4 were also formed. CO production increased and H_2 production decreased by ~7% with increasing NP size. The selectivity trends observed are assigned to possible preferential segregation of Au to the NP surface under reducing reaction conditions, which may be responsible for the low selectivity for hydrocarbon products. In order to further tune the catalytic properties of AuCu NPs, additional studies of the morphological and compositional changes which occur in the NPs under reaction conditions must be performed.

Acknowledgements

This work was funded by the German Federal Ministry of Education and Research (Bundesministerium für Bildung und Forschung, BMBF) under grants 03SF0523A and 03SF0523C – 'CO2EKAT' and the Cluster of Excellence RESOLV at RUB (EXC 1069) funded by the Deutsche Forschungsgemeinschaft. In addition, financial support was provided by the US National Science Foundation (NSF-DMR 1207065). This research used resources of the Advanced Photon Source, a U.S. Department of Energy (DOE) Office of Science User Facility operated for the DOE Office of Science by Argonne National Laboratory (ANL) under Contract No. DE-AC02-06CH11357. MRCAT operations at ANL are supported by the Department of Energy and the MRCAT member institutions. User support at beamline 10-ID-B was provided by Joshua Wright.

Appendix A. Supplementary data

Supplementary data associated with this article can be found, in the online version, at http://dx.doi.org/10.1016/j.cattod.2016.09.017.

References

[1] L. Wang, Y. Yamauchi, Chem.–Asian J. 5 (2010) 2493.
[2] V. Malgras, H. Ataee-Esfahani, H. Wang, B. Jiang, C. Li, K.C.W. Wu, J.H. Kim, Y. Yamauchi, Adv. Mater. 28 (2016) 993.
[3] C. Li, V. Malgras, A. Aldalbahi, Y. Yamauchi, Chem.–Asian J. 10 (2015) 316.
[4] T. Bligaard, J.K. Nørskov, Electrochim. Acta 52 (2007) 5512.
[5] M. Karamad, V. Tripkovic, J. Rossmeisl, ACS Catal. 4 (2014) 2268.
[6] Y. Hori, A. Murata, R. Takahashi, J. Chem. Soc. Faraday Trans. 1 (85) (1989) 2309.
[7] K.P. Kuhl, E.R. Cave, D.N. Abram, T.F. Jaramillo, Energy Eviron. Sci. 5 (2012) 7050.
[8] R. Kortlever, J. Shen, K.J.P. Schouten, F. Calle-Vallejo, M.T. Koper, J. Phys. Chem. Lett. 6 (2015) 4073.
[9] H. Mistry, A.S. Varela, S. Kuehl, P. Strasser, B. Roldan Cuenya, Nat. Rev. Mater. 1 (2016) 16009.
[10] Y. Hori, A. Murata, K. Kikuchi, S. Suzuki, J. Chem. Commun. (1987) 728.
[11] K.P. Kuhl, T. Hatsukade, E.R. Cave, D.N. Abram, J. Kibsgaard, T.F. Jaramillo, J. Am. Chem. Soc. 136 (2014) 14107.
[12] H.A. Hansen, J.B. Varley, A.A. Peterson, J.K. Nørskov, J. Phys. Chem. Lett. 4 (2013) 388.
[13] Y. Li, Q. Sun,Adv. Energy Mater. 6 (2016), article #1600463.
[14] Q. Lu, J. Rosen, F. Jiao, ChemCatChem 7 (2015) 38.
[15] D.R. Kauffman, P.R. Ohodnicki, B.W. Kail, C. Matranga, J. Phys. Chem. Lett. 2 (2011) 2038.
[16] A.A. Peterson, J.K. Nørskov, J. Phys. Chem. Lett. 3 (2012) 251.
[17] H. Hansen, C. Shi, A. Lausche, A. Peterson, J. Nørskov, Phys. Chem. Chem. Phys. 18 (2016) 9194.
[18] P. Hirunsit, W. Soodsawang, J. Limtrakul, J. Phys. Chem. C 119 (2015) 8238.
[19] S. Rasul, D.H. Anjum, A. Jedidi, Y. Minenkov, L. Cavallo, K. Takanabe, Angewandte Chemie 127 (2015) 2174.
[20] X. Guo, Y. Zhang, C. Deng, X. Li, Y. Xue, Y.-M. Yan, K. Sun, Chem. Commun. 51 (2015) 1345.
[21] D. Plana, J. Flórez-Montaño, V. Celorrio, E. Pastor, D.J. Fermín, Chem. Commun. 49 (2013) 10962.
[22] R. Kortlever, I. Peters, S. Koper, M.T. Koper, ACS Catal. 5 (2015) 3916.
[23] M. Watanabe, M. Shibata, A. Kato, M. Azuma, T. Sakata, J. Electrochem. Soc. 138 (1991) 3382.
[24] R. Reske, M. Duca, M. Oezaslan, K.J.P. Schouten, M.T. Koper, P. Strasser, J. Phys. Chem. Lett. 4 (2013) 2410.
[25] A.S. Varela, C. Schlaup, Z.P. Jovanov, P. Malacrida, S. Horch, I.E. Stephens, I. Chorkendorff, J. Phys. Chem. C 117 (2013) 20500.
[26] H.-K. Lim, H. Shin, W.A. Goddard III, Y.J. Hwang, B.K. Min, H. Kim, J. Am. Chem. Soc. 136 (2014) 11355.
[27] J. Christophe, T. Doneux, C. Buess-Herman, Electrocatalysis 3 (2012) 139.
[28] P. Hirunsit, J. Phys. Chem. C 117 (2013) 8262.
[29] D. Kim, J. Resasco, Y. Yu, A.M. Asiri, P. Yang, Nat. Commun. 5 (2014).
[30] D. Friebel, F. Mbuga, S. Rajasekaran, D.J. Miller, H. Ogasawara, R. Alonso-Mori, D. Sokaras, D. Nordlund, T.-C. Weng, A. Nilsson, J. Phys. Chem. C 118 (2014) 7954.
[31] J. Monzó, Y. Malewski, R. Kortlever, F.J. Vidal-Iglesias, J. Solla-Gullón, M. Koper, P. Rodriguez, J. Mater. Chem. A 3 (2015) 23690.
[32] Z. Xu, E. Lai, Y. Shao-Horn, K. Hamad-Schifferli, Chem. Commun. 48 (2012) 5626.
[33] W. Zhao, L. Yang, Y. Yin, M. Jin, J. Mater. Chem. A 2 (2014) 902.
[34] S. Lysgaard, J.S. Mýrdal, H.A. Hansen, T. Vegge, PCCP 17 (2015) 28270.
[35] F. Jia, X. Yu, L. Zhang, J. Power Sources 252 (2014) 85.
[36] N. Artrith, A.M. Kolpak, Nano Lett. 14 (2014) 2670.
[37] C. Schlaup, S. Horch, I. Chorkendorff, Surf. Sci. 631 (2015) 155.
[38] H. Mistry, R. Reske, Z. Zeng, Z.-J. Zhao, J. Greeley, P. Strasser, B.R. Cuenya, J. Am. Chem. Soc. 136 (2014) 16473.
[39] R. Reske, H. Mistry, F. Behafarid, B. Roldan Cuenya, P. Strasser, J. Am. Chem. Soc. 136 (2014) 6978.
[40] C.W. Li, M.W. Kanan, J. Am. Chem. Soc. 134 (2012) 7231.
[41] M. Newville, J. Synchrotron Radiat. 8 (2001) 322.
[42] A. Ankudinov, B. Ravel, J. Rehr, S. Conradson, Phys. Rev. B 58 (1998) 7565.
[43] M. Kuhn, T. Sham, Phys. Rev. B 49 (1994) 1647.
[44] W. Zhu, R. Michalsky, O.N. Metin, H. Lv, S. Guo, C.J. Wright, X. Sun, A.A. Peterson, S. Sun, J. Am. Chem. Soc. 135 (2013) 16833.
[45] S. Back, M.S. Yeom, Y. Jung, ACS Catal. 5 (2015) 5089.
[46] C. Shi, H.A. Hansen, A.C. Lausche, J.K. Nørskov, PCCP 16 (2014) 4720.
[47] A. Pareek, S. Borodin, A. Bashir, G.N. Ankah, P. Keil, G.A. Eckstein, M. Rohwerder, M. Stratmann, Y. Gründer, F.U. Renner, J. Am. Chem. Soc. 133 (2011) 18264.
[48] Y. Tsuda, K. Oka, T. Makino, M. Okada, W.A. Diño, M. Hashinokuchi, A. Yoshigoe, Y. Teraoka, H. Kasai, Phys. Chem. Chem. Phys. 16 (2014) 3815.
[49] H. Liao, A. Fisher, Z.J. Xu, Small 11 (2015) 3221.
[50] E. Voelker, F.J. Williams, E.J. Calvo, T. Jacob, D.J. Schiffrin, Phys. Chem. Chem. Phys. 14 (2012) 7448.
[51] Z.P. Jovanov, H.A. Hansen, A.S. Varela, P. Malacrida, A.A. Peterson, J.K. Nørskov, I.E. Stephens, I. Chorkendorff, J. Catal. (2016) http://dx.doi.org/10.1016/j.jcat.2016.04.008.
[52] X. Liu, A. Wang, L. Li, T. Zhang, C.-Y. Mou, J.-F. Lee, J. Catal. 278 (2011) 288.
[53] A. Wang, X.Y. Liu, C.-Y. Mou, T. Zhang, J. Catal. 308 (2013) 258.
[54] J. Llorca, M. Dominguez, C. Ledesma, R.J. Chimentao, F. Medina, J. Sueiras, I. Angurell, M. Seco, O. Rossell, J. Catal. 258 (2008) 187.
[55] X. Liao, W. Chu, X. Dai, V. Pitchon, Appl. Catal. B: Environ. 142 (2013) 25.
[56] G. Meitzner, G. Via, F. Lytle, J. Sinfelt, J. Chem. Phys. 83 (1985) 4793.
[57] A. Verdaguer-Casadevall, C.W. Li, T.P. Johansson, S.B. Scott, J.T. McKeown, M. Kumar, I.E. Stephens, M.W. Kanan, I. Chorkendorff, J. Am. Chem. Soc. 137 (2015) 9808.
[58] R. Kas, R. Kortlever, A. Milbrat, M.T. Koper, G. Mul, J. Baltrusaitis, PCCP 16 (2014) 12194.
[59] D. Ren, Y. Deng, A.D. Handoko, C.S. Chen, S. Malkhandi, B.S. Yeo, ACS Catal. 5 (2015) 2814.
[60] D. Kim, S. Lee, J.D. Ocon, B. Jeong, J.K. Lee, J. Lee, PCCP 17 (2015) 824.
[61] H. Mistry, A.S. Varela, C. Bonifacio, I. Zegkinoglou, I. Sinev, Y.-W. Choi, K. Kisslinger, E.A. Stach, J.C. Yang, P. Strasser, B. Roldan Cuenya,Nat. Commun. 6 (2016), article # 12123.
[62] Y. Chen, C.W. Li, M.W. Kanan, J. Am. Chem. Soc. 134 (2012) 19969.
[63] J.R. Croy, S. Mostafa, L. Hickman, H. Heinrich, B.R. Cuenya, Appl. Catal. A: Gen. 350 (2008) 207.